AIAA JOURNAL
Vol. 48, No. 9, September 2010

Flame Imaging of Gas-Turbine Relight

R. W. Read,* J. W. Rogerson,† and S. Hochgreb‡
University of Cambridge, Cambridge, England CB2 1PZ, United Kingdom

DOI: 10.2514/1.J050105

High-altitude relight inside a lean-direct-injection gas-turbine combustor is investigated experimentally by high-speed imaging. Realistic operating conditions are simulated in a ground-based test facility, with two conditions being studied: one inside and one outside the combustor ignition loop. The motion of hot gases during the early stages of relight is recorded using a high-speed camera. An algorithm is developed to track the flame movement and breakup, revealing important characteristics of the flame development process, including stabilization timescales, spatial trajectories, and typical velocities of hot gas motion. Although the observed patterns of ignition failure are in broad agreement with results from laboratory-scale studies, other aspects of relight behavior are not reproduced in laboratory experiments employing simplified flow geometries and operating conditions. For example, when the spark discharge occurs, the air velocity below the igniter in a real combustor is much less strongly correlated to ignition outcome than laboratory studies would suggest. Nevertheless, later flame development and stabilization are largely controlled by the cold flowfield, implying that the location of the igniter may, in the first instance, be selected based on the combustor cold flow.

I. Introduction

AMBITIOUS goals have been set to reduce aircraft emissions of nitrogen oxides (NO_x) [1], which contribute to climate change [2] and are harmful to human health [3]. Several engine manufacturers are responding to these challenges by developing next-generation combustion systems based on the lean-direct-injection (LDI) concept. However, the high-velocity fuel-lean conditions that limit NO_x formation in LDI combustors also inhibit the ability to restart the engine at high altitude, making it more difficult to satisfy regulatory requirements [4,5]. Conventional design modifications that improve restart capability often adversely affect other aspects of engine performance by increasing the combustor size, residence time, and cooling requirements. An understanding of the altitude restart process is therefore necessary to optimize overall engine performance while satisfying airworthiness regulations.

In-flight engine restart consists of several distinct phases [6]. First, a spark discharge must generate a viable flame kernel that, in the second phase, must stabilize at a single fuel injector. The process up to this point is referred to as relight, and it is the subject of the present study. To complete engine restart, the flame must then spread around the combustor annulus to all fuel injectors. Lastly, the heat release rate must be sufficient to accelerate the engine spools to their operational speed. Airframe and engine manufacturers typically agree on a maximum restart altitude that ranges from 20,000 to 30,000 ft (6.1 to 9.1 km) above sea level. Following a flameout at 30,000 ft, the combustor inlet temperature, pressure, and air mass flow rate are comparatively low. These conditions combine to impede fuel atomization and chemical reaction, thereby causing large increases in ignition energy requirements and significant reductions in combustion efficiency [6–8]. Despite the unfavorable conditions, engines in service today satisfy restart requirements by generating a low-velocity stoichiometric region adjacent to the spark igniter. While beneficial for restart, stoichiometric mixtures generate comparatively high concentrations of NO_x. Staged combustion systems designed according to the LDI concept achieve NO_x reductions by modifying the equivalence ratio in two or more combustion zones according to the engine thrust requirement. A key difference between a LDI system and a conventional combustor is found in the region between the spark igniter and the fuel injector, where the comparatively high-velocity fuel-lean conditions make LDI relight more difficult. An advanced LDI concept combustor has been studied in this paper.

The physical and chemical processes occurring during relight have been studied previously from several perspectives. Fundamental research has investigated the influence of numerous parameters on the minimum energy associated with flowing, heterogeneous kerosene–air mixtures [7,9,10]. Results indicate that the minimum ignition energy decreases with increasing temperature, pressure, and substoichiometric equivalence ratio, and it increases with turbulence intensity and fuel droplet size. The migration and stabilization of flame during the second phase of relight have also been investigated. Laboratory-scale investigations of methane–air flames using simplified flow configurations and ambient operating conditions have revealed distinct modes of ignition failure and a strong inverse correlation between the gas velocity at the spark electrodes and the probability of ignition success [11,12]. Ignition studies of *n*-heptane spray flames have also demonstrated that the deposited spark energy can have far-reaching spatial effects [13,14]. It remains to be shown whether the simplifications relating to operating temperature and pressure, fuel selection, and injector geometry, inherent in these experimental studies, allow their findings to be extended to the performance of real gas-turbine combustors.

Several practical studies have examined the ignition performance of gas-turbine combustion systems [15–17]. However, published work has been limited to current, conventional combustor designs that differ significantly from LDI technology. Furthermore, no attempt has been made to systematically measure the movement and breakup of flame during altitude relight in a full-scale combustor. Hence, the aims of the present study are as follows:

1) The first aim is to provide insights into the spatial and temporal development of flame during the relight process by analyzing high-speed images in a systematic fashion.

2) The second aim is to identify test-to-test variations in ignition behavior and to investigate differences between successful and unsuccessful ignition events in a real combustor.

3) The third aim is to provide a preliminary assessment of the practical applicability of results derived from laboratory-scale ignition experiments, such as those described in [11–14].

Presented as Paper 2008-0957 at the 46th AIAA Aerospace Sciences Meeting and Exhibit, Reno, NV, 7–10 January 2008; received 28 July 2009; revision received 15 February 2010; accepted for publication 26 March 2010.

*Ph.D. Student, Department of Engineering; currently Postdoctoral Research Associate, Technical University of Denmark, Department of Mechanical Engineering, 2800 Kongens Lyngby, Denmark.

†Postdoctoral Research Associate, Department of Engineering; currently at Doosan Babcock Energy, Research and Development Department, Porterfield Road, Renfrew, Scotland PA4 8DJ, United Kingdom.

‡Professor of Combustion, Department of Engineering. Senior Member AIAA.

To achieve the aims listed previously, a large sample of ignition tests were conducted under high-altitude conditions [18] and analyzed using image-processing software developed for this purpose [19]. The relative strengths of flame convection and propagation are also investigated by comparing the algorithm results with computational fluid dynamics (CFD) predictions of gas-phase velocity.

II. Experimental Method

A. Apparatus

Testing was conducted using the altitude test facility (ATF) at the Rolls–Royce Strategic Research Center, Derby, United Kingdom. The experimental apparatus is illustrated in Fig. 1. A two-sector LDI combustion chamber was mounted inside a pressure vessel with a single fuel injector installed in the sector farthest from the camera. The LDI injector contains a pilot air-blast atomizer that creates a rich mixture close to the centerline; only the pilot is fueled during restart. This atomizer is mounted at the center of several concentric swirlers that create a highly turbulent region of strongly recirculating flow inside the combustor. Details of the design architecture of the injector used in this study are provided in [20].

The jet A kerosene fuel was stored at ambient conditions and supplied in controlled quantities via a mass flow controller. A refrigeration unit and vacuum pump located upstream and downstream of the combustor allowed independent control of air temperature, pressure, and mass flow rate inside the combustion chamber. The two condition set points used during this study are discussed next in Sec. II.B.

Optical access to the combustion chamber was provided by two quartz windows on the near side of the test section (right side in Fig. 1b). The nearside injector was replaced by a vertical slot that created an air curtain to prevent fuel deposition on the combustor window. The slot was sized to match the effective area of the fuel injector. Additional purge air was introduced onto the upstream internal surface of the combustor window to further reduce fuel impingement. Importantly, the purge mass flow rate constituted only a small fraction of the total combustor air at both test conditions, so that the combustor flow patterns were not disturbed by this influx. Warm air was directed over the external surface of the pressure vessel window to prevent condensation.

Sparks were generated by a Champion SK00241 surface-discharge igniter. Introduced from above, the igniter tip was located flush with the outside combustor wall in the injector midplane. The spark energy was supplied by a Unison exciter unit rated to deliver 10 J per spark at a frequency of approximately 1.3 Hz. The peak igniter current and discharge luminosity were measured with a current probe and a photodiode, respectively, and indicated that the spark is relatively consistent, with a standard deviation in each value of less than 8% of the mean.

A Vision Research Phantom camera, situated on the near side of the ATF and viewing roughly perpendicular to the flow direction (Fig. 1b), recorded line-of-sight flame emissions during both successful and unsuccessful ignition events. This nonintensified instrument contained an eight-bit complementary metal-oxide semiconductor, monochrome sensor. The horizontal and vertical pixel resolutions were set to 384 and 256, respectively. Images were recorded at a rate of 5.7 kHz, with an exposure of 165 μs. Although each recording was limited to 1.96 s, the pretrigger interval could be adjusted, and this feature was used to control the timing of each recording relative to the spark (see Sec. II.C). The camera was triggered by a control box that monitored the spark timing and flame luminosity. The spark discharge was identified by a Tektronix TCP303 current probe mounted on the lead joining the exciter unit to the igniter.

The spectral sensitivity of the camera is illustrated in Fig. 2, and it extends from approximately 400 to 1000 nm, with a peak quantum efficiency of 40% at 660 nm. The camera was fitted with a Nikon 28 mm f/2.8 lens that transmitted wavelengths between approximately 350 and 900 nm. The fully stabilized flame brush, produced at the altitude condition defined in this study, is predominately blue in appearance, indicating a strong signal from CH and C_2 chemiluminescence bands (shown in Fig. 2). However, small diffuse regions of yellow light are also evident, confirming the presence of soot. Furthermore, during the ignition event before full flame stabilization, higher levels of soot production might be expected due to the low temperature of the combustor and the large surface-area-to-volume ratio of the developing flame kernel. The blackbody emission from soot particles at an assumed temperature of 2250 K is plotted in Fig. 2 as a fraction of the maximum emission at that

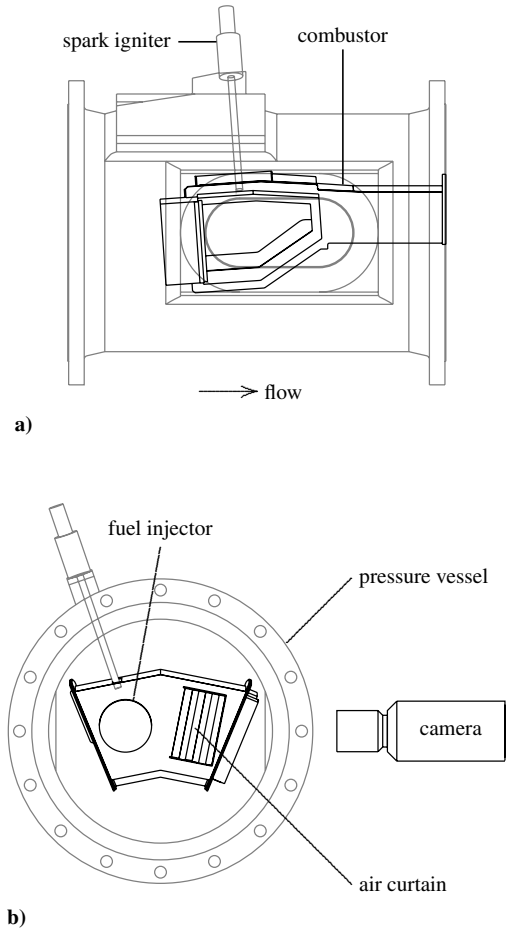

Fig. 1 Test facility: a) view from near side and b) view from upstream.

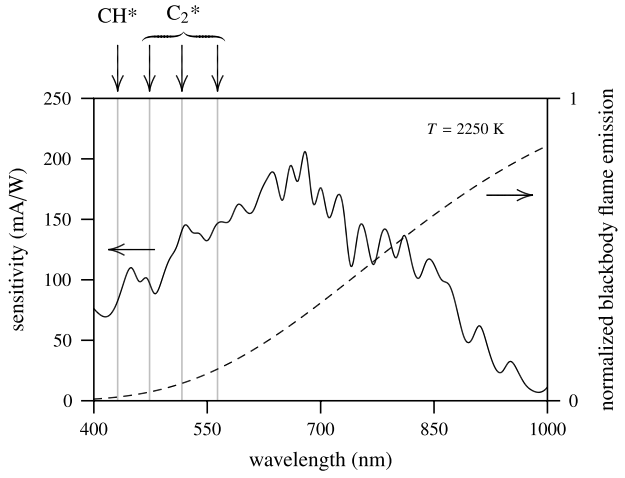

Fig. 2 Spectral sensitivity of the camera (solid line), typical chemiluminescence emission bands (gray vertical lines), and broadband radiation due to soot (dashed line).

Table 1 Low-flow and high-flow condition set points for relight testing

	Low flow	High flow
T_{air}, K	265.0	265.0
P_{air}, kPa	41.4	41.4
T_{fuel}, K	288.0	288.0
FAR[a]	0.030	0.017

[a]FAR denotes fuel-to-air ratio.

temperature. It is therefore likely that the camera signal recorded during ignition is attributable to both chemiluminescence and soot incandescence.

Since the dynamic range of the high-speed camera was limited, and the total flame signal was sometimes weak (see Sec. III.A.1), the decision was made to not attenuate the signal by extracting the chemiluminescence at discrete wavelengths. The light emitted during and shortly following the spark was extremely bright and precluded the use of an intensifier. The camera does not, therefore, record the detailed motion of the flame front per se, but it identifies regions of hot gas either at or reasonably close to the reaction front. In the following sections, the word flame is used in this sense to describe the combined signal arising from both chemiluminescence and soot incandescence.

B. Operating Conditions

Ignition testing was conducted at two high-altitude operating conditions (Table 1) referred to as low flow and high flow, in accordance with the air flow rates at these conditions. The engine manufacturer had previously identified the combustor ignition loop, from which the two set points were selected, so that the low-flow condition lies within the ignition loop and the high-flow condition lies outside the ignition loop (see Fig. 3). Thus, relight can be achieved by sparking repeatedly at the low-flow condition but cannot be achieved at the high-flow condition.

The low-flow set point corresponds to an aircraft flight condition 30,000 ft (9.1 km) above sea level. Conversely, the high-flow set point does not represent a flight condition but is a test point at the same temperature and pressure as the low-flow condition that is routinely used to characterize the ignition performance of the combustor. The sole difference between the two operating conditions is the larger air mass flow rate at the high-flow point. This influences the ignition process in two respects. First, as the air flow rate through an air-blast atomizer increases, a finer fuel spray is generated. The minimum energy required to ignite a droplet spray increases markedly with drop size [9,21]. A larger airflow might therefore be expected to favor ignition. However, the second effect of an increased air flow rate is to impair flame stabilization by reducing the residence time and increasing the aerodynamic strain [6]. At the low-flow condition, these effects combined to produce successful relight for approximately 17% of the sparks.

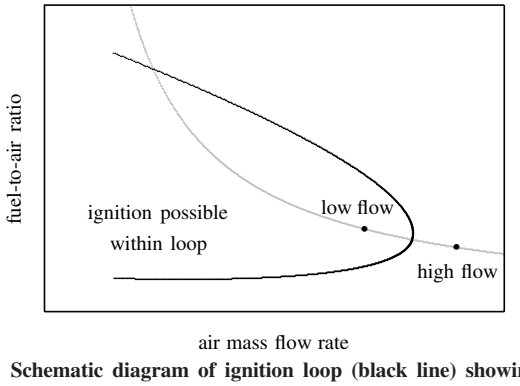

Fig. 3 Schematic diagram of ignition loop (black line) showing the positions of the test points along a curve of constant fuel flow rate (gray line). The ignition loop separates regions of successful and unsuccessful relight.

Table 2 Number of high-speed recordings

	Low flow	High flow
Success	94	——
Failure	101	93

C. Test Procedure

Numerous ignition tests were conducted as follows. The required air temperature, pressure, and mass flow rate were generated in the test facility. Following stabilization of these conditions, fuel was admitted into the combustion chamber through the pilot atomizer. The ignition system was activated after 2 s and thereafter generated a spark every 750 ms until the test was terminated.

At the low-flow operating condition, sparks were generated until flame was detected, whereupon the camera was triggered. During a single ignition test, the largest number of sparks required to achieve success was 14. Having selected an appropriate pretrigger recording interval, the high-speed images captured the successful ignition event and the previous unsuccessful attempt. At the high-flow operating point, the camera was triggered on the first spark and captured three ignition attempts before the test was terminated. A delay of 60 s between tests ensured the dispersion of liquid fuel that accumulated in the bottom of the combustion chamber. Approximately 100 high-speed recordings were obtained for each of three categories: success, low-flow failure, and high-flow failure (Table 2). A larger sample size might have revealed more pronounced differences between successful and unsuccessful ignition events. However, the collected samples were sufficient to provide insight into several important features of the relight process.

D. Flame-Tracking Algorithm

The results of the experiment consist of a series of high-speed sequences of images, and the analysis of these images seeks to extract information in a systematic way, so that overall trends and characteristic behaviors may be identified. The objective of the algorithm developed here is to identify regions of flame activity in

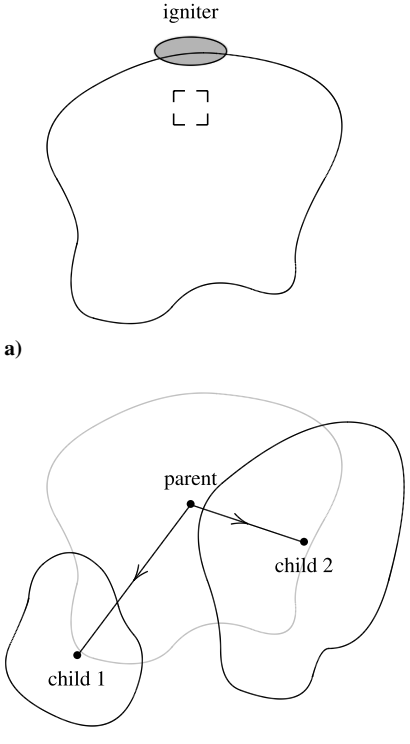

Fig. 4 Flame-tracking process: a) first frame and b) second frame.

each image and associate them with the detected activity in the previous image. In this way, the important aspects of flame behavior are revealed: namely, movement, splitting, and combination of the detected objects. The initial motion and breakup of the spark kernel are monitored according to the process illustrated in Fig. 4. The extent of the spark is identified in the opening frame by a threshold-based search, starting from a small predefined area below the igniter tip (see dashed box). The following frame is then searched to identify child flame objects in the area formerly occupied by the parent spark kernel. This process is repeated for subsequent frames, on each occasion noting the parents of any detected flame objects. By recording the intensity-weighted centroid of every object, it is possible to construct a trajectory map, as demonstrated next.

The implementation of this flame-tracking algorithm is complicated by several factors, and these were addressed directly by developing the software to handle the most difficult cases. Three characteristics of the flame emission during relight required special attention: 1) large variations in signal intensity with time, 2) fast-moving small fragments splitting away from identified flame objects, and 3) complete loss of signal during some tests.

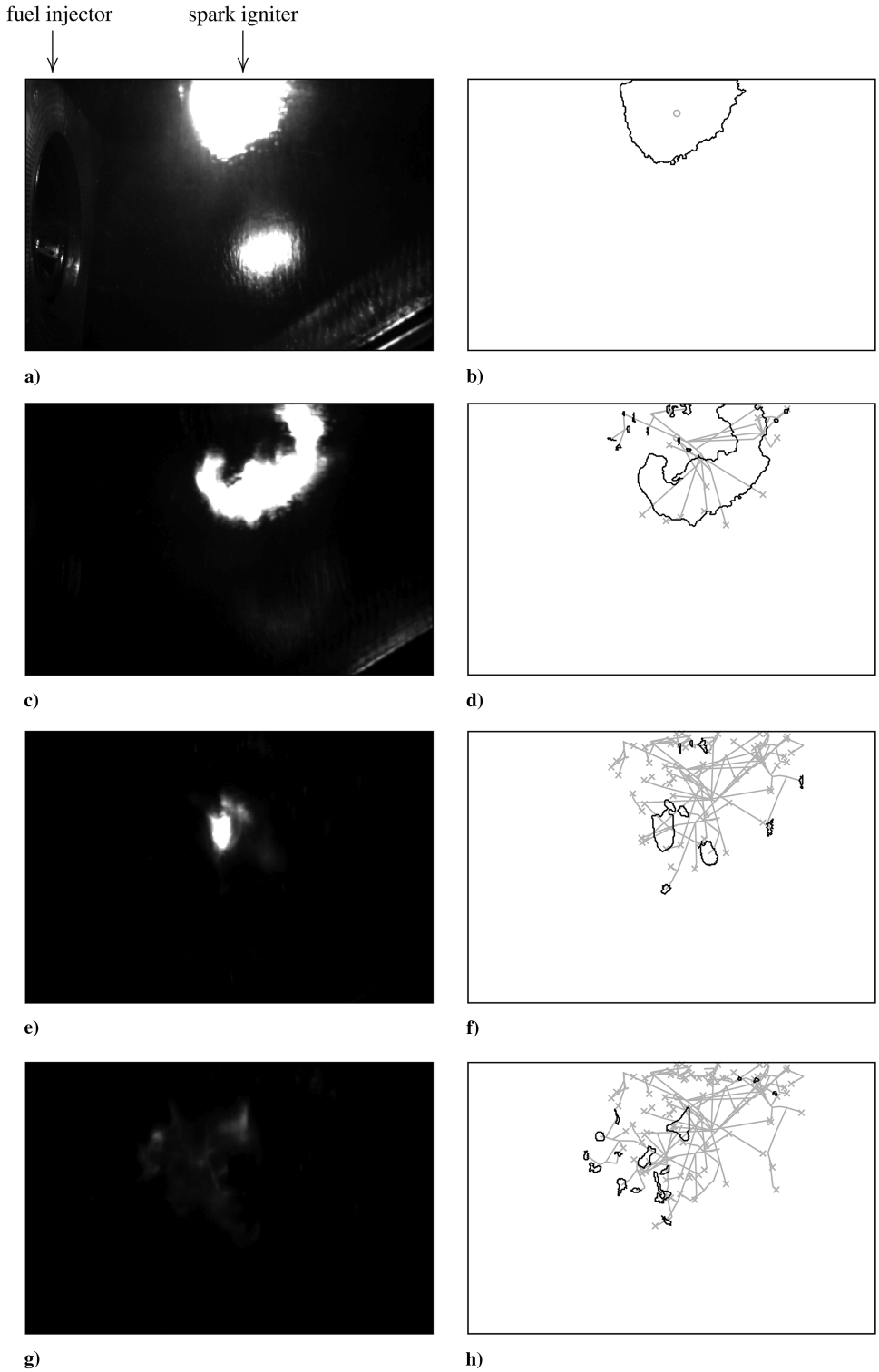

Fig. 5 High-speed images of an ignition test and corresponding flame object trajectories at time t ms following spark: a and b) $t = 0.3$, c and d) $t = 1.9$, e and f) $t = 3.5$, and g and h) $t = 5.1$.

The first difficulty is that the measured signal intensity varies significantly throughout each ignition event. As illustrated in Fig. 5a, the spark is extremely bright, producing a well-defined area of saturated signal around the igniter tip and generating strong reflections on the wet combustor walls. In contrast, during later development, small faint objects are observed separating from larger volumes of flame. These low-intensity fragments often grow later during the relight process, and it is important for the tracking program to retain them. An adaptive threshold is therefore required to ensure that bright spark reflections are not classified as flame, while regions of faint flame are successfully identified. This threshold is taken as

$$I_{\text{thr}} = pI_{\max} \tag{1}$$

where $p = 0.5$ and $I_{\max}$ is the maximum count in the parent flame object. Note that the parameter p in Eq. (1) controls the extent of each identified object but changing its value does not significantly affect observed trends in the results.

A second difficulty is produced by small faint regions of flame. These fragments are often ejected from an object at comparatively high velocities. Following the process illustrated in Fig. 4, a fast-moving child could move beyond the boundary of its parent and thus be lost. To avoid this, the search region is expanded by a fixed number of pixels, and a second low-threshold search is conducted. This is illustrated in Fig. 6, where C_1 is a bright object lying within the bounds of its parent and easily identified by the procedure described previously, whereas C_2 is a fainter, more distant body requiring identification. An expanded region is searched for pixels with a nonzero signal (no noise was apparent) and, on discovering such a pixel at x_i, the threshold is immediately reset,

$$I_{\text{thr}} = \max\{I_{\text{thr}}, pI(x_i)\} \tag{2}$$

and a new child is constructed. If C_1 is encountered during this build, the threshold is reset to remove the pixels in the current child with the lowest count:

$$I_{\text{thr}} = I_{\min} \tag{3}$$

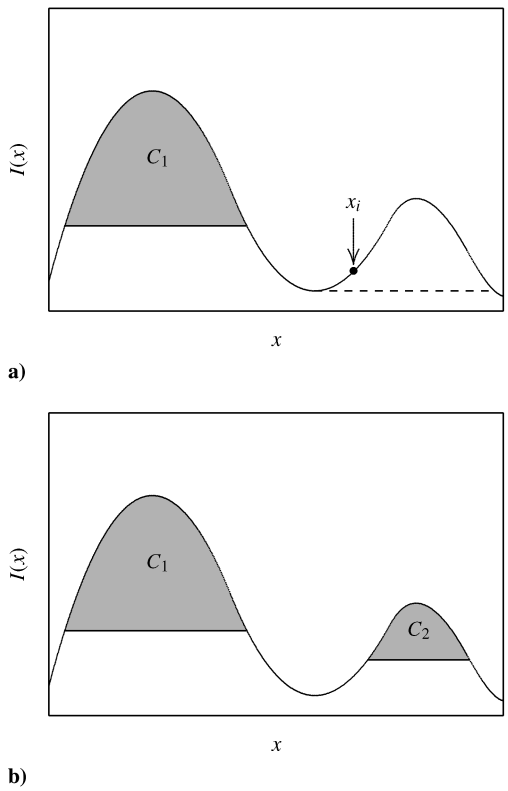

Fig. 6 Identification of ejected object: a) initial search and b) final build.

This threshold is repeatedly reset until either the generating point x_i is itself excluded (i.e., it cannot be separated from C_1) or the new child is separated from C_1 (see dashed line in Fig. 6a). The new child is then examined to determine whether $I_{\min} > pI_{\max}$, where $I_{\max}$ is the maximum pixel count contained in the new child. If this condition is satisfied, then the child build is complete; otherwise, the threshold is again reset,

$$I_{\text{thr}} = pI_{\max} \tag{4}$$

and the final build commences at the brightest pixel, resulting in the identification of the flame object C_2, as shown in Fig. 6b. The adaptive threshold and expanding search features successfully capture low-level activity, but they also tend to produce flame objects with a large number of parents from the previous image. Unsuitable associations are therefore eliminated to produce a clearer illustration of flame movement. An apparent link is only included if the distance between the parent and the child is comparatively small (no more than twice that from the closest parent to that child) and the parent is comparatively large (no less than half the size of the largest parent).

A third problem results from loss of signal being detected by the camera. While only a handful of the successful recordings exhibit complete loss of signal, approximately half include images containing no pixels with counts exceeding one (out of a maximum of 255). These low-intensity episodes typically occur for a period of less than 1 ms, between 10 and 20 ms, following the spark. When the flame activity is lost in this way the program conducts a low-threshold search in subsequent frames until a new object is identified, whereupon the tracking process continues as described previously. Consequently, although breaks in the trajectory plot occasionally occur, the program is able to track successful events throughout the 25 ms analysis period.

Figure 5 shows a series of flame emission images together with the corresponding object outlines (black) and trajectory history (gray) generated by the tracking algorithm. Note that the trajectories are drawn between the intensity-weighted centroids of identified flame objects in sequential images. The bulk flow is from left to right, and the center of the spark kernel is identified in Fig. 5b by an unfilled gray circle. Note that the strong reflections apparent in Fig. 5a are not identified as flame in Fig. 5b, having been excluded by the initial search procedure, as described previously. Every gray line represents the path of an individual flame object. Fragmentation and merging of these objects is represented by branching and recombination of the lines, respectively. The disappearance of an object following extinction is indicated by a cross. As the sequence proceeds, it is observed that a large number of small fragments are identified by the algorithm. Many of these extinguish almost immediately but, in some cases, the fragments grow and recombine into a larger flame body. Figures 5g and 5h show that the algorithm has identified bright parts of the flame correctly, but this does not imply that these objects are completely separate.

III. Results and Discussion

A. Preliminary Observations

The total intensity variation measured by the camera in each high-speed recording provides a simple assessment of combustion activity during ignition. A preliminary analysis used these data to characterize the timescales of ignition success and failure and to investigate the behavior of stabilized flame.

1. Timescales of Success and Failure

The total intensity traces plotted in Fig. 7a are typical examples of ignition success and failure. The high-intensity initial signal, due to the spark, decreases to a low level within approximately 5 ms. This large reduction in flame emission has been observed in previous gas-turbine ignition studies [16,22]. During the low-intensity delay period before recovery or failure, the successful and unsuccessful plots are indistinguishable, and flames that later grow and develop successfully emit very little light at this point. Indeed, during six of the 94 successful recordings, the flame emissions were so weak that

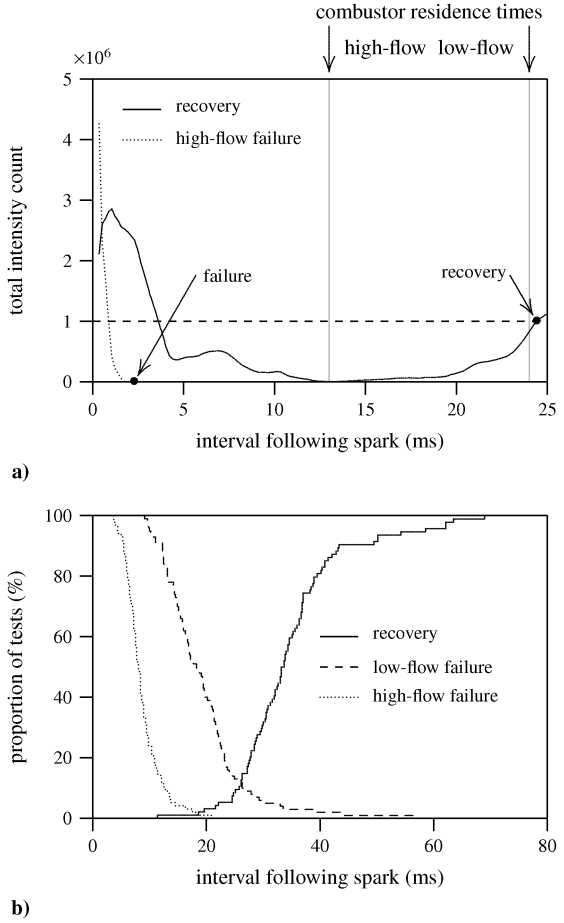

Fig. 7 Timescales of success and failure: a) sample total intensity traces at the two conditions and b) cumulative statistics.

the camera registered no signal whatsoever. These false failures typically occurred for a period of less than 1 ms and resulted from either a dramatic reduction in flame volume or a shift in the emission wavelength to beyond the detection range of the imaging system (see Fig. 2 for the spectral sensitivity of the high-speed camera).

The failure and recovery times used to characterize each test outcome, and frequently referred to next, are also illustrated in Fig. 7a for typical failed and successful ignitions. The failure time is defined as the interval between the spark and the last frame containing any flame activity. The recovery time is the period following the spark when the signal first increases to exceed a threshold value of 1×10^6 counts (see dashed line in Fig. 7a). The intensity count never exceeds this value during a failure, but it always recovers strongly after having exceeded it during a successful attempt.

The characteristic times of every ignition event are compiled in Fig. 7b. This plot illustrates the proportion of unsuccessful tests that are yet to fail (dashed and dotted lines) and the fraction of successful tests that have already recovered (solid line). For a given condition and outcome, the range of recovery and failure times is large when compared with the mean. This is particularly true during successful events, when the low-intensity phase before recovery can be as short as 10 ms or can persist for a period of up to 69 ms. This suggests that recovery is a random event not strictly correlated with the operating conditions at the instant of the spark.

It is clear from Fig. 7b that failures occur faster at the high-flow condition than at the low-flow point. Indeed, 67% of high-flow failures occur before the first low-flow failure. Although the cumulative curves of failure times have similar profiles in Fig. 7b, the flame development process is observed to be quite different for low-flow and high-flow failures. When viewed directly, the sequence of high-speed images indicates that high-flow failures result from disintegration of the spark kernel, whereas low-flow failures generally occur following significant flame propagation. These two

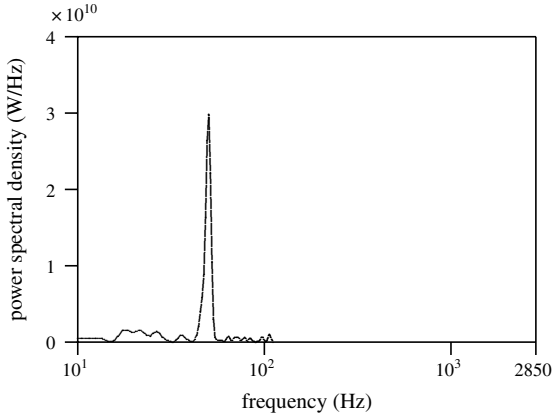

Fig. 8 Periodicity of established flame.

modes of failure have also been observed during ignition studies of laboratory-scale flames, where the operating conditions differ substantially from those inside a combustor [12]. This important observation is explored further in Sec. III.B.

2. *Periodicity of Established Flame*

Visual examination of the high-speed images acquired following flame recovery suggests that the stabilized flame fluctuates roughly sinusoidally. These fluctuations are associated with cyclic changes in the total area of detected objects rather than variations in their luminosity. Fourier analysis of the total flame intensity signal indicates a strong peak in power at a frequency of 50.5 Hz, as shown in Fig. 8. To minimize spectral leakage, a single Hamming window was applied to the time series before performing a discrete Fourier transform (DFT) [23]. The length of the DFT was set to 11,400 points, thereby providing a spectral resolution of 0.5 Hz (f_s= 5.7 kHz). Virtually all of the power is contained in frequencies of less than 100 Hz. This is also true for many of the stabilized flame signals recorded following recovery. The Fourier analysis was repeated for the 88 successful ignition events that generated a continuous signal between 150 and 540 ms. All of these signals demonstrate maximum power spectral densities at frequencies of less than or equal to 60 Hz. Indeed, half have their maximum at between 50 and 55 Hz. This fluctuation of steady-state flame may either be combustion induced or could result from a 50 Hz instability generated in the cold flow before the spark.

Thermoacoustic oscillations result from the positive feedback between pressure and heat release that can occur inside a gas-turbine combustion chamber. Aircraft engine spray flames are susceptible to low-frequency rumble instabilities at idle and subidle conditions

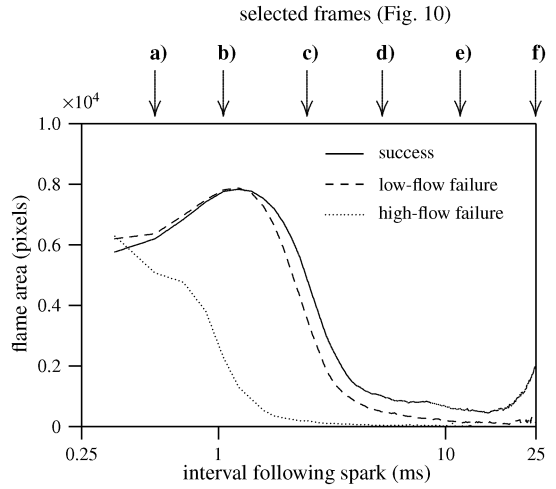

Fig. 9 Evolution of mean flame area based on all recorded ignition tests. Note that the horizontal axis is logarithmic.

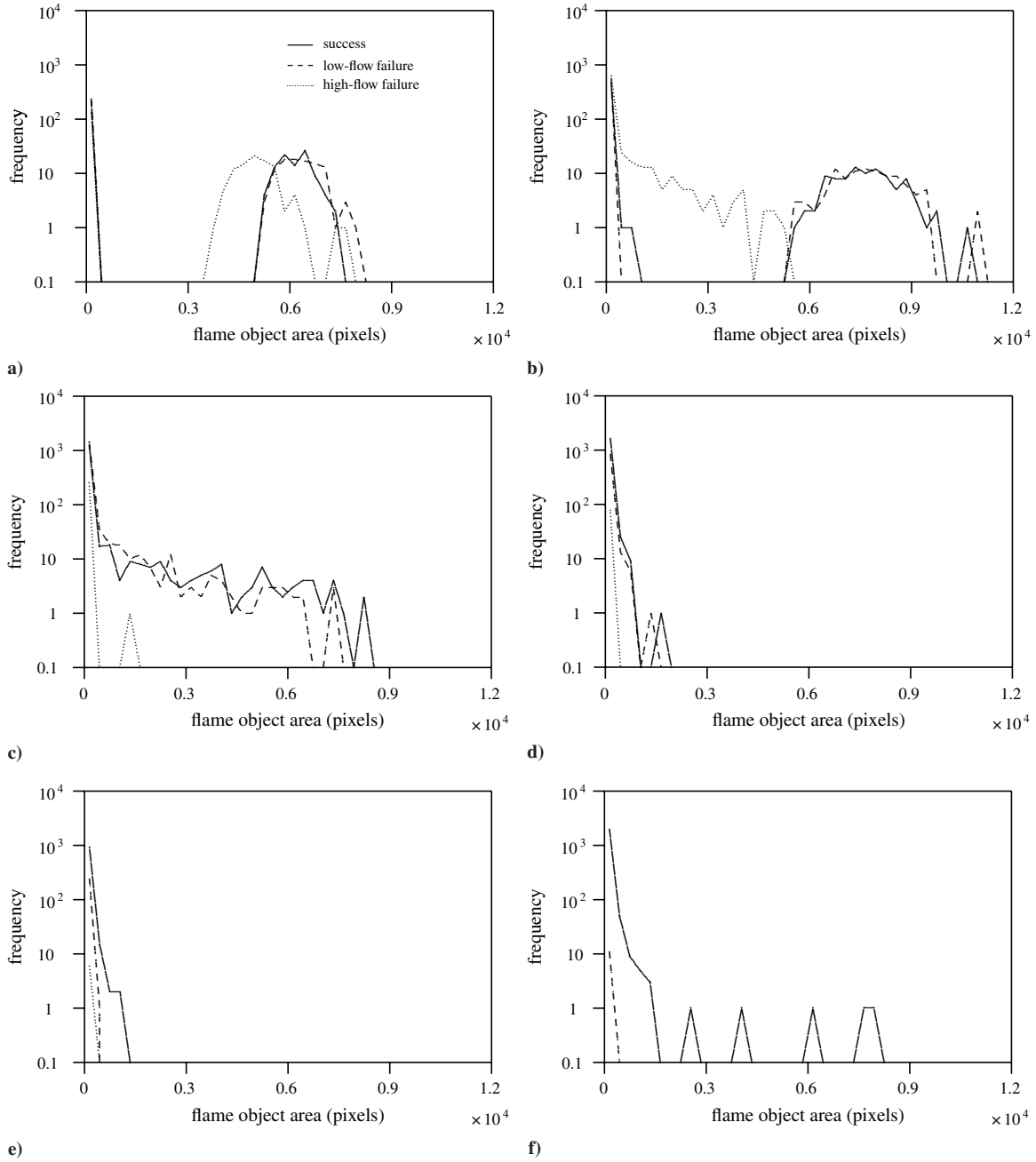

Fig. 10 Evolution of flame object area at time t ms following spark: a) $t = 0.5$, b) $t = 1.1$, c) $t = 2.5$, d) $t = 5.3$, e) $t = 11.6$, and 5) $t = 24.9$.

[24]. Previous work reported in [25] has shown that these frequencies typically extend from 50 to 120 Hz, encompassing a large proportion of the frequencies observed in the present study.

The observed fluctuations may alternatively be caused by a cold flow instability. A previous study of isothermal flow through a fuel injector has demonstrated that induced swirl can generate instabilities at low frequencies [26]. If such a cold instability is causing the flame oscillations in the present study, then it may be possible to improve the ignition probability by firing the spark at a particular point in the cycle. The present results show no consistent relationship between the phase of the spark, relative to the most powerful intensity sinusoid, and the number of successful events. However, a larger sample size would be required to draw a definitive conclusion.

B. Flame-Tracking Results

The variations in flame object size, trajectory, and velocity revealed by the tracking algorithm provide valuable information concerning the relight process and permit investigation of the systematic differences between successful and unsuccessful ignition events.

1. Spark Kernel Disintegration

The flame-tracking program records the size of all identified flame objects. By summing the size of every object contained in a single image, the variation in recorded flame area during each ignition event can be identified. Note that the trends observed in the flame area data are reproduced by plotting the means of either the maximum intensity or total intensity contained in each flame object, indicating that the choice of flame area to reveal characteristic behaviors is not critical. The area extracted from each image does not correspond to the flame surface area, and it also differs from the number of active pixels in the frame, as the tracking program excludes all reflections. Having grouped all of the tests into three categories of success, low-flow failure, and high-flow failure, the means of their imaged areas calculated by the algorithm are plotted as a function of time in Fig. 9.

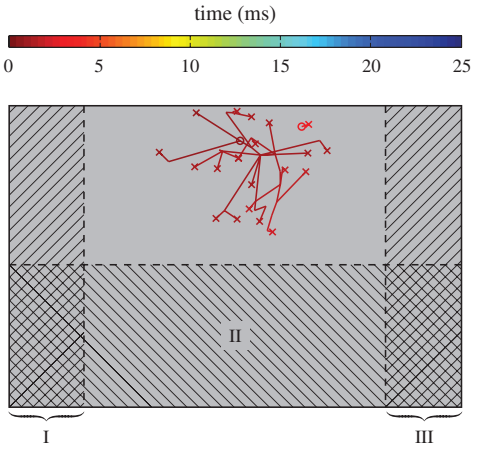

a)

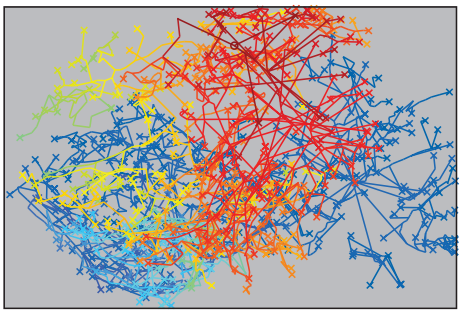

b)

Fig. 11 Sample flame trajectory plots: a) high-flow failure and b) success.

The mean plots illustrate several important features of relight flame development. The mean counts associated with the spark kernel at the earliest times are very similar; this implies that the spark kernel size plays no role in determining ignition outcome and is not influenced by the change in test conditions. Immediately following the spark, the area occupied by flame increases at the low-flow condition. This is due to the hot kernel expanding. In contrast, rapid quenching of the spark at the high-flow set point causes the pixel count to decrease monotonically with time. After approximately 2 ms, the area at the low-flow condition begins to decrease rapidly, suggesting that the flame fails to liberate sufficient heat to survive. The difference between successes and failures at the low-flow condition is insignificant when compared with the sample standard deviation (Fig. 10) and only becomes larger after approximately 20 ms, when the earliest instances of flame recovery begin.

The area distributions of individual flame objects generated during all events are plotted in Fig. 10 at six intervals following the spark. These times were selected to ensure that the subfigures are separated regularly in logarithmic time, as shown in Fig. 9. At all intervals following the spark, very small objects are present in significantly greater numbers than large objects, requiring the use of a logarithmic vertical axis in Fig. 10. In each subplot, a large degree of scatter is apparent in the data, again highlighting variability in the ignition process. Figure. 10a, at 0.5 ms, shows plots of the flame object size distributions extracted from the second frame following the spark. At both test conditions, a Gaussian distribution of large objects and a collection of small fragments are apparent. The disparity between the initial size distribution at the two set points can be attributed to early flame growth at the low-flow condition. This initial growth is also apparent in Fig. 10b, at 1.1 ms, where the success and low-flow failure histograms are again indistinguishable from each other. Breakup of the initial kernel into smaller bodies is clearly evident in the high-flow histogram at this stage. In Fig. 10c, at 2.5 ms, the number of high-flow tests starts to decrease due to ignition failures. At this point, low-flow detected objects also exhibit the breakup behavior first observed at the high-flow condition (cf., Fig. 10b). Figures 10d and 10e, at 5.3 and 11.6 ms, respectively, indicate that, during the low-intensity period before recovery, flame at the low-flow condition separates into a collection of small fragments. The growth apparent in Fig. 10f, at 24.9 ms, is associated with the early stages of recovery during a small number of tests.

2. *Flame Trajectories*

Having observed that the distributions of flame object sizes are similar for successes and low-flow failures up to 25 ms, it remains to be seen whether their spatial developments inside the combustor are different and whether the test condition affects them. Trajectory plots corresponding to a high-flow failure and a successful relight are illustrated in Fig. 11. The total intensity variations associated with these two specific tests were plotted previously in Fig. 7a. Both plots in Fig. 11 are color coded with respect to time, progressively changing from dark red to dark blue during a period of 25 ms following the spark.

The high-flow trajectory plot displayed in Fig. 11a shows that the spark kernel disintegrates rapidly, with little opportunity for the flame to spread upstream. This fast breakup, seen in all high-flow recordings, results from the increased flow velocities and turbulence intensities generated at the high-flow test condition, and it is reflected in the comparatively fast flame breakup, highlighted in Sec. III.B.1. Figure 11b is typical of the flame development maps associated with many successful ignition events. Following initial activity below the igniter tip, flame moves upstream before developing strongly in the lower upstream quadrant of the combustion chamber.

The relationship between flame migration and ignition success has been investigated by calculating the proportion of tests registering flame activity in three overlapping regions, labeled I, II, and III in Fig. 11a. Region I is an upstream portion of the image close to the fuel injector, region II contains all points below the injector centerline, and region III is a downstream area close to the combustor exit. The statistics obtained from the tracking program are listed in Table 3.

The vast majority of successful ignition events register flame activity in all three regions of the combustion chamber during the 25 ms following the spark. Most low-flow failures also register activity below the centerline and at the combustor exit. However, approximately half of these failed attempts display no evidence of flame at the fuel injector during the first 25 ms. This result indicates that, although flame movement onto the injector face is a prerequisite for successful ignition, it does not guarantee success; at least 55% of failures occur having achieved this. Furthermore, as illustrated in Fig. 12a, the distribution of times required for flame to enter the fuel-injector region (i.e., region I) is similar for successful and unsuccessful ignition events. This implies that those unsuccessful flames that enter the injector region are transported or propagate at a similar rate to objects that are ultimately successful. Note the extremely broad range of these detection times, indicating the highly stochastic nature of ignition. Figure 12b illustrates the distribution of the intensity count contained within these flame objects as they cross into the upstream region. Again, they are similar, indicating that there is no difference between the intensity of those flame objects first reaching the fuel injector during successful and unsuccessful ignition events.

At the high-flow condition, flame is observed below the fuel-injector centerline in less than half of the ignition attempts, and signal is recorded at the injector face in virtually no cases. Disintegration of the initial flame kernel occurs so rapidly at the high-flow set point that failure occurs before flame can be transported into regions I and II.

Table 3 Percentage of tests registering flame activity in specific regions (see Fig. 11a)

	Success	Low-flow failure	High-flow failure
I: Upstream	100	55	3
II: Below centerline	99	89	44
III: Downstream	86	85	74

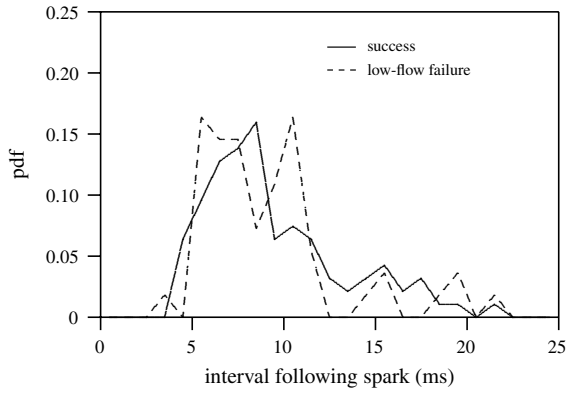

a)

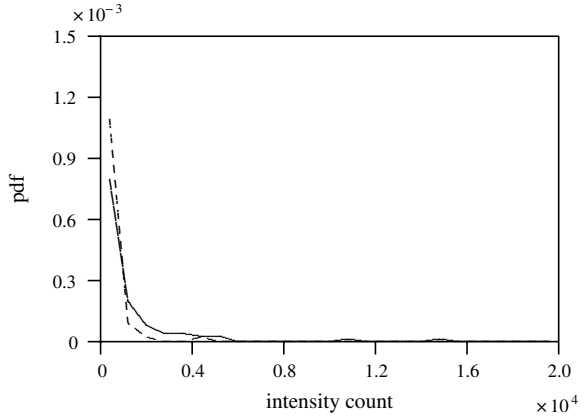

b)

Fig. 12 Probability densities of detected objects entering region I: a) crossing time and b) intensity delivery.

However, the downstream convection of the early flame is sufficiently fast to generate a signal at the exit during the majority of high-flow failures.

Although all high-flow ignition failures occur in a similar manner, low-flow unsuccessful events fail in a variety of ways. Figure 13 consists of four trajectory plots, each representing a different mode of low-flow failure. Although upstream flame motion is clearly required for successful relight, flame is also observed leaving the combustion chamber downstream. This convective loss of flame occurs during many low-flow tests, and it is sometimes directly responsible for a failure. The four low-flow failure modes are in contrast to the high-flow failure in Fig. 11a, which disintegrates with little propagation. The flame-tracking program thus confirms the visual observations of failure categories, reported earlier in Sec. III.A.1.

The experiments in [12] identified three types of failures in a laboratory-scale flame. The first failure identified was a spark followed by no indication of flame initiation, which most resembles a high-flow failure in the current study but could also broadly describe the low-flow failure mode in Fig. 13a. This is a comparatively rare event at the low-flow condition. The second failure identified was flame initiation followed by downstream blowoff, which is analogous to Fig. 13b. The third failure identified was flame propagation and momentary stabilization before extinction, exemplified by Fig. 13d. As noted previously, roughly half of low-flow ignition failures register flame movement onto the injector face and therefore fall into this category. These similarities in ignition failure mode observed in the laboratory experiment and the combustor measurements occur despite significant differences in the operating temperature and pressure, fuel selection, and injector geometry. The low-flow failure in Fig. 13c represents a failure mode that has not been previously reported, namely, a split in the initial kernel followed by downstream blowoff with simultaneous upstream propagation.

3. *Spark Kernel Velocities*

CFD modeling of the combustor airflow has been performed by Rolls–Royce, plc. to develop an understanding of the cold flowfields at the low-flow and high-flow set points. A nonreacting large-eddy simulation (LES) was conducted using the Rolls–Royce corporate combustion program, PRECISE. The modeling implemented in this code is described in [27]. The geometry and boundary conditions defined in the model were not identical to those of the test facility but, instead, corresponded to a single sector with periodic boundary conditions (i.e., representing a full combustor annulus). The time-averaged results of the simulation nonetheless provide a useful comparison with the mean velocities measured in the experiment.

Three streamlines generated by the cold LES and passing below the igniter tip are illustrated in Fig. 14. The mean spark centroid and the igniter tip are represented by open and filled circles, respectively.

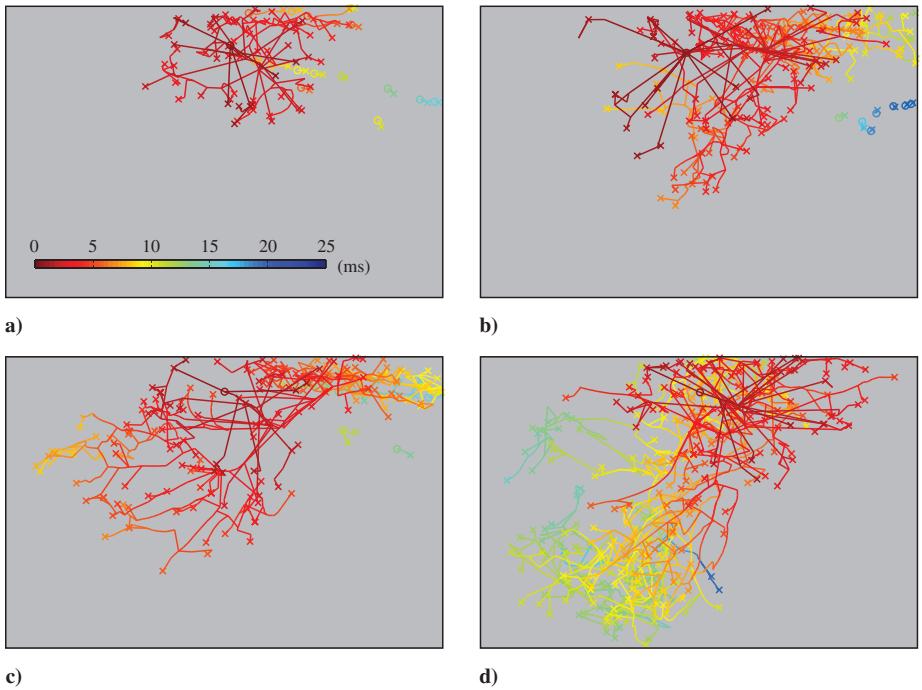

a) b)

c) d)

Fig. 13 Modes of low-flow failure: a) rapid disintegration, b) flame exit, c) flame split, and d) no stabilization at injector.

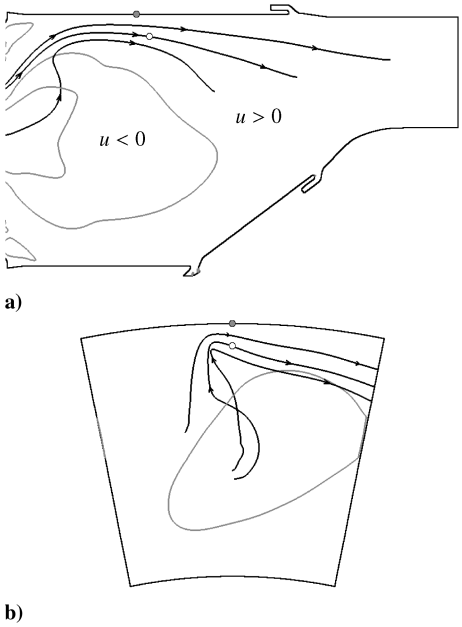

Fig. 14 Time-averaged, cold CFD simulation at the low-flow condition, showing streamlines and central recirculation zone: a) view from near side and b) view from downstream.

The zero contours of axial velocity are also shown in gray. The streamlines terminate on the side of the computational domain, indicating that the swirl component of velocity is comparable in magnitude to the axial velocity. A well-developed recirculation zone is apparent in the upstream portion of the combustion chamber, bounded by the gray lines. This recirculation is responsible for transporting developing flame toward the fuel injector and is therefore necessary to ensure flame stabilization. A corridor of high-velocity air separates the igniter tip from this region, and a significant part of the flame kernel must traverse this corridor to enable stabilization. At the low-flow condition, the velocities immediately below the igniter are lower, and the spark kernel is sufficiently large to ensure that early flame is delivered into the recirculation zone and successfully transported upstream (Fig. 5).

As noted earlier, the tracking software records the centroid locations of every flame body. It is therefore possible to estimate the spark kernel velocity between the first and second frames and to make a direct comparison with the CFD results. Tables 4 and 5 present a comparison of the measured spark velocity and the CFD-predicted gas-phase velocity at the average spark-centroid location. The spark velocity calculation includes a correction for the oblique viewing angle of the high-speed camera. The measured velocities therefore describe spark motion in the central plane of the combustor sector. Although the camera cannot detect offplane motion of the flame, the CFD predictions of swirl velocity u_θ have been included. These values demonstrate that, while there is significant swirl, the axial component of velocity is dominant.

Notwithstanding the differences in geometry and boundary conditions, the velocities u_z and u_r show reasonable agreement between the CFD predictions and the results of the flame-tracking algorithm. An exception occurs for the radial velocity u_r at the low-flow condition (See Table 4), where the flame-tracking algorithm indicates a much higher velocity than the CFD (−8.7 m/s when compared with −2.8 m/s for the CFD). As previously observed, high-flow failure is caused by rapid disintegration of the spark body, with no evidence of kernel growth (see Sec. III.B.1). At the high-flow set point, the initial kernel therefore follows the flow, resulting in broad agreement with the cold flow CFD (see Table 5). In contrast, significant flame growth occurs at the low-flow condition before breakup. While upward growth of the kernel is prevented by the combustor outside wall, the flame is unconstrained from below. The centroid of flame activity therefore descends faster than the flowfield, as demonstrated in Table 4.

Previous studies have demonstrated that high local velocities at the spark location produce a lower probability of ignition: for example, during ignition of a turbulent nonpremixed methane jet [11]. This suggests that ignition outcome in the ATF may depend on the local air velocity at the igniter tip. However, as shown in Table 6, there is only a small difference between the mean axial velocities for success and failure, and the difference in means is negligible when compared with the standard deviations associated with the two categories. Therefore, although the higher levels of turbulent straining associated with large velocities below the igniter undoubtedly inhibit flame development, this is not the dominant factor determining ignition outcome in a practical combustor. The conditions during the spark are less influential, because the time required for flame stabilization or failure is generally longer inside a practical combustor than in laboratory experiments. This may be associated with the lower temperature and pressure inside the combustor (ambient conditions during laboratory experiment), with the choice of fuels (methane in laboratory or jet A kerosene in combustor), or with a difference in the flow timescales between the two configurations.

4. Evolution of Velocity Field

Employing the same method used to find the spark kernel velocity, the velocities of flame objects have been identified during the later stages of successful ignition events. Velocity data derived from the flame-tracking program were spatially and temporally averaged, and they were constructed into a series of vector maps, illustrating the general motion of the flame. Vector maps constructed from recordings of successful ignition events are presented in Fig. 15.

These vectors represent the three-dimensional motion of flame that may occupy any point across the width of the combustor. Ascribing a magnitude to these velocities therefore implies the projection of all velocity vectors onto the central plane of the combustor sector. Each vector represents the average velocity of objects in an imaged area of 3.8×3.8 mm, during 0.88 ms. A velocity vector is displayed at locations where at least 10 flame objects are contained in the averaging square. The flame motion illustrated in these figures is due to both convection and flame propagation relative to the gas phase.

Figure 15a illustrates the initial flame centroid velocities averaged over the interval from 0.4 to 1.2 ms following the spark. Here, the mean velocity field is similar to that recorded for the individual tests, since the spark is localized and has not yet disintegrated. The pocket of hot gas generated by the spark discharge moves downstream and toward the fuel-injector centerline at relatively high velocities. Shortly following the spark, successful ignition is characterized by

Table 4 Spark kernel and CFD velocities at low-flow condition, m/s

	u_z	u_r	u_θ
Flame	21.1	−8.7	——
CFD	17.5	−2.8	−7.6

Table 5 Spark kernel and CFD velocities at high-flow condition, m/s

	u_z	u_r	u_θ
Flame	32.8	−2.8	——
CFD	33.2	−4.3	−11.8

Table 6 Spark kernel streamwise velocities at low-flow condition, m/s

	Mean	Std. dev.
Success	20.2	5.8
Low-flow failure	21.8	6.9

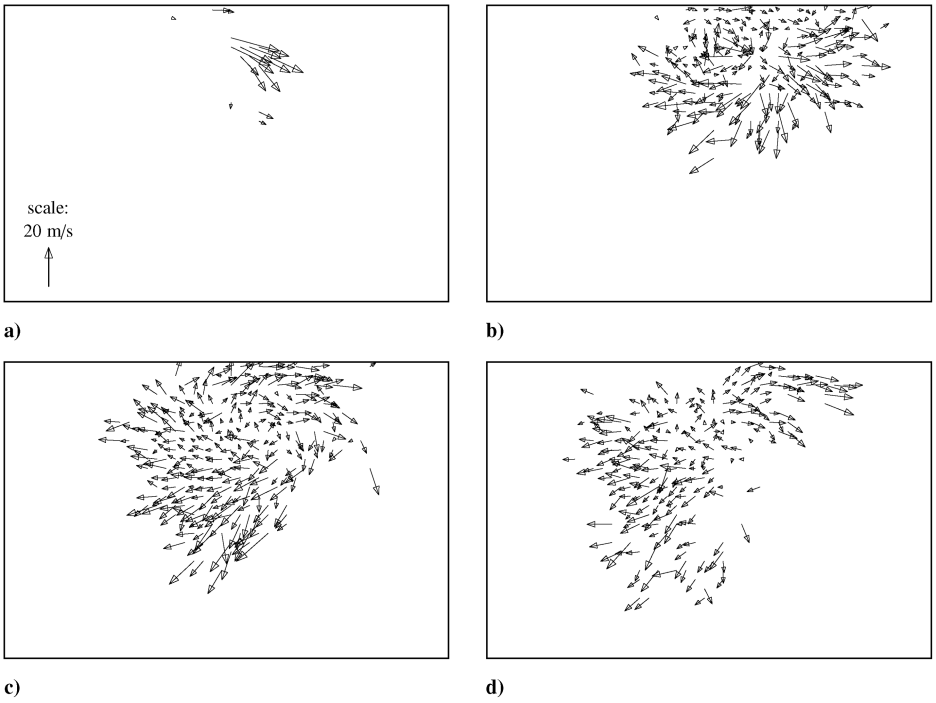

Fig. 15 Mean flame object velocity for successful tests (all at the low-flow condition) at $t \pm 0.4$ ms following spark: a) $t = 0.8$, b) $t = 2.5$, c) $t = 4.3$, and d) $t = 6.1$.

upstream flame motion back toward the fuel-injector face, as shown in Figs. 15b–15d. Note that the velocity fields at these time intervals are constructed from many small flame objects moving in all directions after the disintegration of the spark kernel. However, a clear structure of recirculation can be seen from the means, and separate regions of upstream and downstream flame movement are clearly evident.

Figure 16 illustrates the flame centroid velocities averaged over the 25 ms following the spark. The plot is broadly representative of flame motion in the combustion chamber, as distinct regions of the chamber tend to register flame activity at different times (Fig. 15). The flame activity moves predominantly upstream in the region to the left of the igniter, confirming the presence of a large recirculation zone. Flame objects downstream of the igniter move toward the combustor exit. A significant region of downward flame motion is generated by swirl. The measured flame motion illustrated in Figs. 15 and 16 is in agreement with the structure of the time-averaged CFD results, seen previously in Fig. 14. The upstream flame velocity vectors coincide with the CFD recirculation zone, suggesting that flame motion is dominated by convection rather than propagation. It is reasonable to conclude that the combustor flow patterns at the low-flow set point tend to promote stabilization of flame at the injector face, provided that the air mass flow rate does not prohibit kernel survival. In addition, these findings suggest that cold LES can identify the smallest distance between the igniter tip and the recirculation zone, thus providing useful guidance regarding igniter placement.

IV. Conclusions

In this study, experiments were performed in an ATF to increase understanding of ignition and flame development during relight of a LDI combustor. An image-processing algorithm was developed to analyze the motion and breakup of flame during relight, allowing the construction of a single flame trajectory plot representing each ignition attempt. This algorithm may be further employed in future

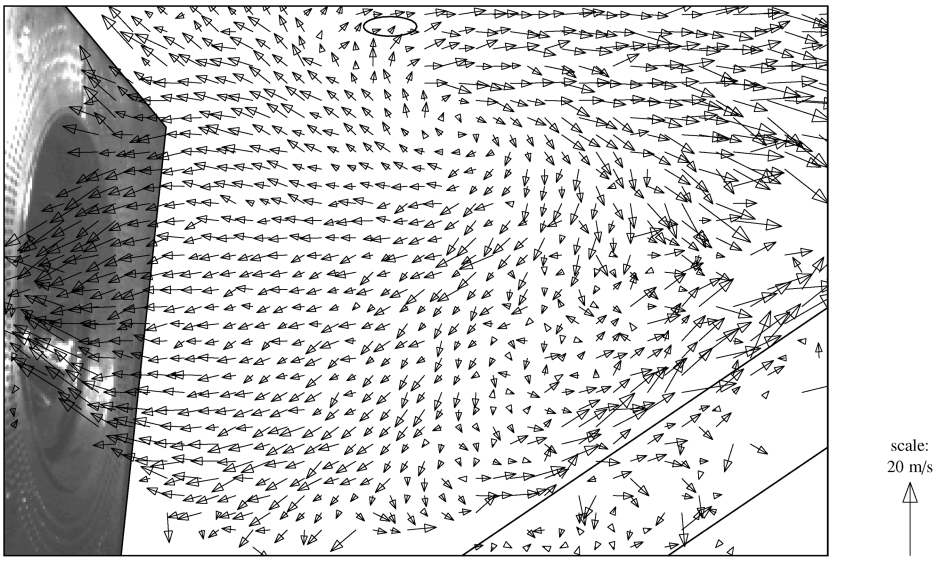

Fig. 16 Mean flame object velocity for successful tests (all at the low-flow condition) averaged over 25 ms following spark.

work to analyze ignition phenomena encountered in situations ranging from simplified laboratory experiments to realistic engine studies.

The trajectory plots revealed several modes of relight failure occurring in a full-scale gas-turbine combustor that are the same as those previously identified for a laboratory-scale burner. On the other hand, initial kernel velocities are found to have a much smaller influence on ignition outcome than suggested by laboratory-scale experiments. This result demonstrates that, although many laboratory studies are performed, they do not always represent the complex processes occurring inside practical combustors. High-quality measurements inside gas-turbine combustion systems are therefore required to complement more fundamental laboratory experiments. The analysis of many high-speed images has demonstrated that the spark kernel disintegrates rapidly during the early stages of relight, and the initial kernel velocities show good agreement with CFD predictions of the cold flow. Finally, flow patterns apparent from measuring the average velocity of hot gases were similar to cold CFD results, implying that flame motion is dominated by convection rather than propagation. The study therefore suggests that cold flow simulations are a good starting point for identifying the ideal location for the igniter.

Acknowledgments

The project was sponsored by Rolls–Royce, plc. and the United Kingdom Department of Trade and Industry, under the ATAP-10 program. R. W. Read acknowledges the support of the Engineering and Physical Sciences Research Council's industrial cooperative awards in science and engineering and collaborative training account awards. S. Hochgreb acknowledges additional support from the Royal Society in the form of a Wolfson Merit Award. The authors would like to thank Rolls–Royce, plc. for providing access to their altitude relight test facility and for their generous technical assistance. Particular thanks to C. Goddard and M. Zedda of the Rolls–Royce Combustion Systems Department for providing the computational fluid dynamics data. We would also like to thank E. Mastorakos for the loan of the high-speed camera used during this study.

References

[1] "Strategic Research Agenda 1" Vol. 2, Advisory Council for Aeronautics Research in Europe, Brussels, 2002.

[2] Penner, J. E., Lister, D. H., Griggs, D. J., Dokken, D. J., and McFarland, M. (eds.), *Aviation and the Global Atmosphere*, Cambridge Univ. Press, Cambridge, England, U.K., 1999.

[3] Kampa, M., and Castanas, E., "Human Health Effects of Air Pollution," *Environmental Pollution*, Vol. 151, No. 2, 2008, pp. 362–367. doi:10.1016/j.envpol.2007.06.012

[4] "Restart Capability," Federal Aviation Regulation, Pt. 25, Sec. 903(3), 2009.

[5] "Relighting in Flight," *Certification Specifications for Engines*, Sec. CS-E 910, European Aviation Safety Agency, Cologne, Germany, 2003.

[6] Lefebvre, A. H., *Gas Turbine Combustion*, 2nd ed., Taylor and Francis, Philadelphia, 1999.

[7] Ballal, D. R., and Lefebvre, A. H., "Ignition and Flame Quenching of Flowing Heterogeneous Fuel–Air Mixtures," *Combustion and Flame*, Vol. 35, 1979, pp. 155–168. doi:10.1016/0010-2180(79)90019-1

[8] Caines, B. N., Hicks, R. A., and Wilson, C. W., "Influence of Sub-Atmospheric Conditions on the Performance of an Airblast Atomiser," 37th AIAA/ASME/SAE/ASEE Joint Propulsion Conference, AIAA Paper 2001-3573, July 2001.

[9] Rao, K. V. L., and Lefebvre, A. H., "Minimum Ignition Energies in Flowing Kerosine–Air Mixtures," *Combustion and Flame*, Vol. 27, Aug.–Dec. 1976, pp. 1–20. doi:10.1016/0010-2180(76)90002-X

[10] Ballal, D. R., and Lefebvre, A. H., "Ignition of Liquid Fuel Sprays at Subatmospheric Pressures," *Combustion and Flame*, Vol. 31, 1978, pp. 115–126. doi:10.1016/0010-2180(78)90122-0

[11] Ahmed, S. F., and Mastorakos, E., "Spark Ignition of Lifted Turbulent Jet Flames," *Combustion and Flame*, Vol. 146, Nos. 1–2, 2006, pp. 215–231. doi:10.1016/j.combustflame.2006.03.007

[12] Ahmed, S. F., Balachandran, R., Marchione, T., and Mastorakos, E., "Spark Ignition of Turbulent Nonpremixed Bluff-Body Flames," *Combustion and Flame*, Vol. 151, Nos. 1–2, 2007, pp. 366–385. doi:10.1016/j.combustflame.2007.06.012

[13] Marchione, T., Ahmed, S. F., Balachandran, R., and Mastorakos, E., "Effectiveness of Localised Spark Ignition in Recirculating *n*-Heptane Spray Flames," 21st International Colloquium on the Dynamics of Explosions and Reactive Systems, Poitiers, France, July 2007.

[14] Marchione, T., Ahmed, S. F., and Mastorakos, E., "Ignition of Turbulent Swirling *n*-Heptane Spray Flames Using Single and Multiple Sparks," *Combustion and Flame*, Vol. 156, No. 1, 2009, pp. 166–180. doi:10.1016/j.combustflame.2008.10.003

[15] Xiong, T., Huang, Z., and Wang, Y., "Some Factors Affecting Altitude Relighting Performance of Turbojet Engine Combustor," American Society of Mechanical Engineers Paper 81-GT-49, Fairfield, NJ, 1981.

[16] Naegeli, D. W., and Dodge, L. G., "Ignition Study in a Gas Turbine Combustor," *Combustion Science and Technology*, Vol. 80, No. 4, 1991, pp. 165–184. doi:10.1080/00102209108951784

[17] Pucher, G., and Allan, W. D., "Turbine Fuel Ignition and Combustion Facility for Extremely Low Temperature Conditions," *Proceedings of the ASME Turbo Expo*, Vol. 1, American Society of Mechanical Engineers, Fairfield, NJ, 2004, pp. 385–392.

[18] Read, R. W., "Experimental Investigations into High-Altitude Relight of a Gas Turbine," Ph.D. Thesis, Univ. of Cambridge, Cambridge, England, U.K., 2008.

[19] Read, R. W., Rogerson, J. W., and Hochgreb, S., "Relight Imaging at Low Temperature, Low Pressure Conditions," 46th AIAA Aerospace Sciences Meeting and Exhibit, AIAA Paper 2008-957 , Jan. 2008.

[20] Buelow, P. E. O., Williams, B. P., Bretz, D. H., Spooner, M., Mohamed, C., and Gill, H., U.S. Patent Application Publication No. 2006/0248898 A1 for "Lean Direct Injection Atomizer for Gas Turbine Engines," 2006.

[21] Ballal, D. R., and Lefebvre, A. H., "Ignition and Flame Quenching of Quiescent Fuel Mists," *Proceedings of the Royal Society of London, Series A: Mathematical and Physical Sciences*, Vol. 364, No. 1717, 1978, pp. 277–294. doi:10.1098/rspa.1978.0201

[22] Pucher, G., Wang, G., Bardon, M. F., Gardiner, D. P., Namet-Allah, A. M., and Benaissa, A., "Enhanced Ignition Systems for Aircraft Altitude Relight," *48th Annual Conference of the Canadian Aeronautics and Space Institute*, Vol. 48, Canadian Aeronautics and Space Institute, Kanata, Ontario, Canada, 2001, pp. 611–620.

[23] Press, W. H., Teukolsky, S. A., Vetterling, W. T., and Flannery, B. P., *Numerical Recipes: The Art of Scientific Computing*, 3rd ed., Cambridge Univ. Press, New York, 2007.

[24] Zhu, M., Dowling, A. P., and Bray, K. N. C., "Self-Excited Oscillations in Combustors with Spray Atomizers," *Journal of Engineering for Gas Turbines and Power*, Vol. 123, No. 4, 2001, pp. 779–786. doi:10.1115/1.1376717

[25] Eckstein, J., Freitag, E., Hirsch, C., and Sattelmayer, T., "Experimental Study on the Role of Entropy Waves in Low-Frequency Oscillations in a RQL Combustor," *Journal of Engineering for Gas Turbines and Power*, Vol. 128, No. 2, 2006, pp. 264–270. doi:10.1115/1.2132379

[26] Carrotte, J. F., and Batchelor-Wylam, C., "Characterisation of the Instantaneous Velocity and Mixture Field Issuing from a Lean-Premixed Module (LPM)," *Proceedings of the ASME Turbo Expo*, Vol. 2, American Society of Mechanical Engineers, Fairfield, NJ, 2003, pp. 489–498.

[27] James, S., Zhu, J., and Anand, M. S., "Large-Eddy Simulations as a Design Tool for Gas Turbine Combustion Systems," *AIAA Journal*, Vol. 44, No. 4, 2006, pp. 674–686. doi:10.2514/1.15390

R. Lucht
Associate Editor